Current Research in Structural Biology 8 (2024) 100157

Contents lists available at ScienceDirect

Current Research in Structural Biology

journal homepage: www.journals.elsevier.com/current-research-in-structural-biology

Research Article

Structural insights into the initiation of free radical formation in the Class Ib ribonucleotide reductases in Mycobacteria

Lumbini R. Yadav [a], Vasudha Sharma [b], Maheswaran Shanmugam [b], Shekhar C. Mande [a,c,*]

[a] National Centre for Cell Science, SPPU Campus, Ganeshkhind, Pune, 411007, India
[b] Department of Chemistry, Indian Institute of Technology Bombay, Powai, Mumbai, 400076, Maharashtra, India
[c] Bioinformatics Centre, Savitribai Phule Pune University, Ganeshkhind, Pune, 411007, India

ARTICLE INFO

Handling Editor: Prof G Oliva

Keywords:
RNRs -ribonucleotide reductase
Mtb-*Mycobacterium tuberculosis*
Mth-*Mycobacterium thermoresistibile*
Tyr-free radical
NrdF2I- NrdF2: NrdI complex

ABSTRACT

Class I ribonucleotide reductases consisting of α and β subunits convert ribonucleoside diphosphates to deoxyribonucleoside diphosphates involving an intricate free radical mechanism. The generation of free radicals in the Class Ib ribonucleotide reductases is mediated by di-manganese ions in the β subunits and is externally assisted by flavodoxin-like NrdI subunit. This is unlike Class Ia ribonucleotide reductases, where the free radical generation is initiated at its di-iron centre in the β subunits with no external support from another subunit. Class 1b ribonucleotide reductase complex is an essential enzyme complex in the human pathogen *Mycobacterium tuberculosis* and its structural details are largely unknown. In this study we have determined the crystal structures of Mycobacterial NrdI in oxidised and reduced forms, and similarly those of NrdF2:NrdI complexes. These structures provide detailed atomic view of the mechanism of free radical generation in the β subunit in this pathogen. We observe a well-formed channel in NrdI from the surface leading to the buried FMN moiety and propose that oxygen molecule accesses FMN through it. The oxygen molecule is further converted to a superoxide ion upon electron transfer at the FMN moiety. Similarly, a path for superoxide radical transfer between NrdI and NrdF2 is also observed. The oxidation of Mn(II) in NrdF2I to high valent oxidation state (either Mn(III) or Mn(IV) assisted by the reduced FMN site was evidently confirmed by EPR studies. SEC-MALS and low resolution cryo-EM map indicate unusual stoichiometry of 2:1 in the *M. tuberculosis* NrdF2I complex. A density close to Tyr 110 at a distance <2.3 Å is observed, which we interpret as OH group. Overall, the study therefore provides important clues on the initiation of free radical generation in the β subunit of the ribonucleotide reductase complex in *M. tuberculosis*.

1. Introduction

Reduction of ribonucleoside di-/tri phosphates into deoxyribonucleoside di-/tri phosphates is one of the most fundamental biochemical steps in all life forms (Jordan and Reichard, 2003). Ribonucleotide reductases (RNRs), which catalyse this step, use a unique free radical mechanism for the conversion. RNRs have been classified into three distinct classes depending upon the cofactor they use, the radicals that mediate the catalytic reaction and so on. Among the RNRs, Class I RNRs typically consist of two subunits, α and β, where the α subunits mediate the catalytic conversion of ribonucleosides into deoxyribonucleosides, whereas free radical generation happens in the β subunits (Cotruvo and Joanne, 2008). The Class I ribonucleotide reductases have further been classified into Class Ia- Ie, based on multiple factors including metallocofactor that they use, allosteric regulation and accessory proteins they utilize (Nordlund and Reichard, 2006; Torrents, 2014, ; Ruskoski and Boal, 2021). Class Ia RNR β subunits use Fe to facilitate generation of Tyr• radical in presence of oxygen, whereas in Class Ib RNR's β subunits need external assistance from NrdI protein, and generate the Tyr• radical mediated by Manganese, and Oxygen (Roca et al., 2008; Cotruvo and Joanne, 2008). Large number of elegant biochemical and structural studies have revealed different aspects of free radical transfer and utilization during the enzymatic cycle (Nordlund et al., 1990; Hammerstad et al., 2014; John et al., 2022). Moreover, structural studies have also been important in enhancing our understanding of the allosteric regulation mechanisms in different RNRs (Thomas et al., 2019; Zimanyi et al., 2016; Brignole et al., 2018).

Mycobacterium tuberculosis (Mtb) possess Class Ib RNR gene cluster

* Corresponding author. National Centre for Cell Science, SPPU Campus, Ganeshkhind, Pune, 411007, India.
E-mail addresses: shekhar@nccs.res.in, shekhar.mande@gmail.com (S.C. Mande).

https://doi.org/10.1016/j.crstbi.2024.100157
Received 24 April 2024; Received in revised form 8 August 2024; Accepted 16 September 2024
Available online 18 September 2024

(NrdHIEF2) that is essential for growth. Apart from this cluster, multiple genes for the β subunits, namely nrdF1 (class 1b-like) and nrdB (class 1c-like) are also present (Mowa et al., 2009). Class Ib RNR in Mycobacteria have therefore been considered to be attractive drug targets. Class Ib genes in prokaryotes are encoded by the *nrdE*, *nrdF* and *nrdI*, with other accessory genes such as the *nrdH*. The *nrdE* and *nrdF* genes in Class Ib RNRs and their homologs *nrdA* and *nrdB* in Class Ia RNRs are more generally referred to as the α and β subunits. Although the catalytic cycle of conversion of ribonucleoside di-phosphate to deoxyribonucleoside di-phosphate happens in the NrdE subunits of Class Ib RNRs, free radical generation using atmospheric oxygen occurs at the di-metal binding site of the NrdF2 subunit assisted by the NrdI subunit.

Much work using structural, biochemical and spectroscopic studies has been carried out to enhance our understanding of the Class Ia RNRs, especially that related to radical transfer between α and β subunits over a long range, and the mode of regulation by nucleotides. Mechanisms of these are likely to be similar in Class Ib RNRs (Eriksson et al., 1997; Zimanyi et al., 2016; Kang et al., 2020; Lin et al., 2017). Moreover, $O_2^{\bullet-}$ mediated assembly of Mn^{III} Mn^{IV} intermediate in Class Ib RNR and consequent Tyr• radical formation has also been observed experimentally (Cotruvo et al., 2013). We present here crystal structures of NrdI in oxidised and reduced forms at a resolution of 1.2 Å, and those of binary complexes of NrdF2 and NrdI (NrdF2I) at a resolution of 3 Å. The structural and spectroscopy analysis clearly outlines the early steps in free radical generation in the Mtb RNR.

2. Results

Our goal has been to uncover the structural details and mechanistic features of Mycobacterial RNR subunits. Employing X-ray crystallography and other biophysical techniques, we have characterized the structures of *Mycobacterium thermoresistibile* (Mth) NrdI, which is a close homolog of the corresponding Mtb subunit and Mtb NrdF2: NrdI (NrdF2I) complex, in both their oxidised and reduced forms. Our work enhances the understanding of the free radical generation process in Class Ib RNR's.

2.1. Structural analysis of NrdI

The structure of *Mycobacterium thermoresistibile* (Mth) NrdI was determined at 1.2 Å resolution in its oxidised and reduced forms (Supplementary Table 1). The structure is similar to other reported NrdI structures with canonical flavodoxin-like fold (Fig. 1A). The root mean square deviation (RMSD) among the available structures of NrdI reveals comparable conformational features among all the structures (Supplementary Table 2).

Electron density for FMN is present at its canonical binding site in the pockets formed by 40s, 50s and 80s loops termed according to the flavodoxin (FLDs) nomenclature (Sancho, 2006) (Fig. 1A). The isoalloxazine ring of FMN is stacked between residues Phe 92 on one side and Tyr 49 on the other. Phe 92 demonstrates a parallel displaced π-π interaction while Tyr 49 shows parallel staggered interaction with FMN (McGaughey et al., 1998; Ali et al., 2022). Tyr 49 is conserved in all the reported NrdI structures, while phenylalanine or tryptophan residues are observed at position-92. These non-bonded π-π interactions are also observed in other NrdI structures and play a role in stabilisation of the isoalloxazine ring of FMN in the binding pocket, electron transfer during oxidation-reduction, and may also have a role in promoting interaction responsible for molecular assembly with NrdF2.

The major conformational change between the oxidised and reduced structures is around the isoalloxazine ring, where a peptide flip at Gly 50 is seen in the reduced form. This is similar to that observed in other reported structures of NrdI (Johansson et al., 2010; Asmund Kjendseth Røhr et al., 2010; Boal et al., 2010). The peptide flip leads to the

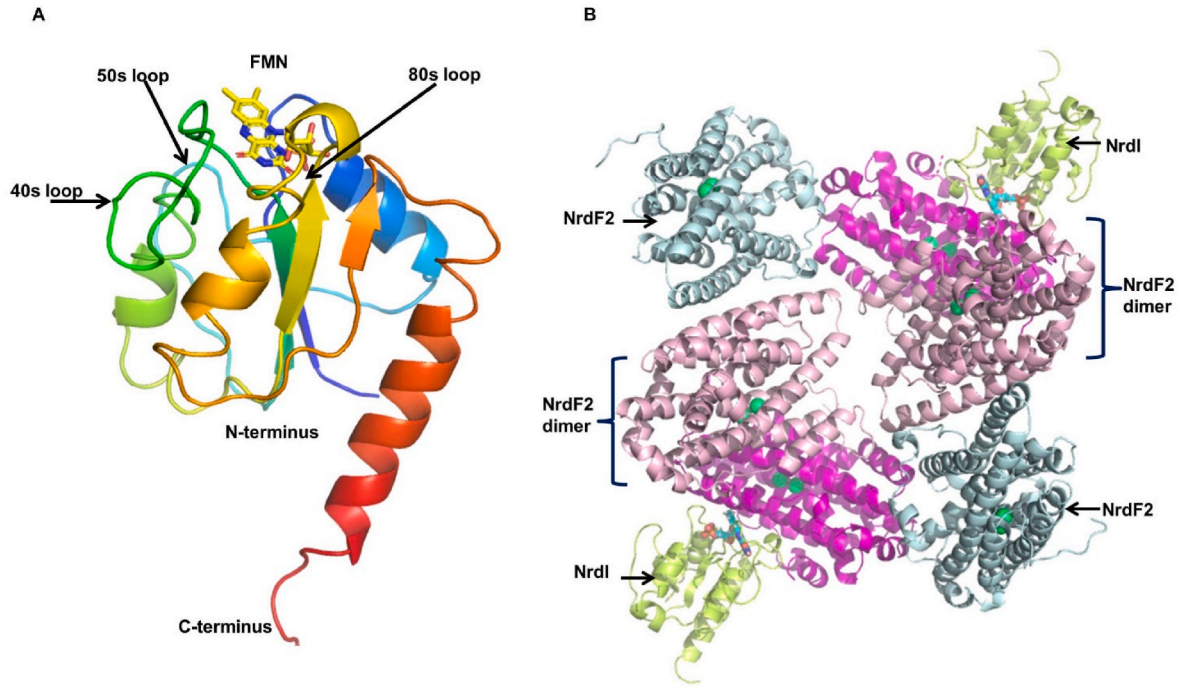

Fig. 1. Overview of structure of Mth NrdI and Mtb NrdF2I complex: (A) The overall structure of Mth NrdI shown in cartoon representation. The chain has been color-coded from blue to red starting from N-terminal to C-terminal. The important features of the structure, namely the 50s loop, 40s loop and 80s loop are indicated. These loops not only make important contacts with the FMN moiety, but also participate in association with NrdF2. **(B)** Structure of MtbNrdF2I complex: 6 chains of NrdF2 and 2 of NrdI were observed in the crystal asymmetric unit. The stoichiometry of the complex was such that two chains of the dimer of NrdF interacted with one chain of NrdI. NrdF chain which is not part of physiological dimer is colored as palecyan. The functional part of asymmetric unit which is dimer of NrdF2 is colored as hotpink and lightpink while a single NrdI monomer is colored as limongreen. Bound metal ions in NrdF2 are shown in limegreen. (For interpretation of the references to color in this figure legend, the reader is referred to the Web version of this article.)

formation of a hydrogen bond between carbonyl oxygen of Gly 50 and N5 atom of FMN (Supplementary Fig. 1C).

2.2. Structural analysis of Mtb NrdF2I complex

The structures of Mtb NrdF2I complexes in reduced and oxidised forms were determined at ~3 Å resolution (Supplementary Table 1). Missing density for 32 C-terminal residues in NrdF2 is similar to reported structures of NrdF2 from other organisms (Uppsten et al., 2004; Eriksson et al., 1998; Högbom et al., 2002). The Mtb NrdF2I complex structures superpose with the reported Class Ib structures with a RMSD of 1.0 and 0.6 Å for *B. cereus* (PDB ID 4BMO) and *E. coli* (PDB ID 3N39) respectively and 0.8 Å for Class Ie *A. urinae* (PDB ID 7MMP) structure (Supplementary Table 3). Thus, the overall conformational features in all the complexes are similar, but with a difference in their stoichiometry (Supplementary Fig. 2).

2.2.1. Stoichiometry of interaction

The asymmetric unit of NrdF2I complex structure comprises of six chains of NrdF2 and two chains of NrdI (Fig. 1B). NrdF is known to exist as a dimer in solution and therefore buried surface area analysis was used to identify the physiologically relevant dimer. Accessible surface area calculations revealed that areas buried between different NrdF2 chains were 2000 and 850 $Å^2$ respectively. Thus, the two NrdF2 chains with buried surface area of 2000 $Å^2$ represent the physiological dimer. Further buried surface area was also used to assess complex formation between NrdF2 and NrdI (Yan et al., 2008). The dimer of NrdF2 interacts with NrdI by burying area of 1000 $Å^2$ (Protein interfaces, surfaces and assemblies service PISA at the European Bioinformatics Institute; Krissinel and Kim, 2007). The two chains of NrdI in asymmetric unit associate with two physiological dimers of NrdF2 in the crystal asymmetric unit (Fig. 1B). The stoichiometry of interaction in the Mtb NrdF2I complex structure therefore is 2:1 unlike other reported structures where the stoichiometry has been observed to be 1:1. Crystal packing examination indicated possibility of a clash if the stoichiometry were 1:1. The position where the other NrdI subunit would be placed in such a 1:1 complex is occupied by another NrdF2 subunit in our asymmetric unit. Further confirmation of 2:1 stoichiometry was sought through experiments including SEC-MALS analysis, which also suggested stoichiometry of 2:1 (Supplementary Fig. 3A). Similarly, low resolution cryo-EM map obtained of Mth NrdF2I structure suggested the stoichiometry of the complex to be 2:1 (Supplementary Fig. 3B).

Glutaraldehyde crosslinking studies were also performed to confirm stoichiometry of complex. The molecular weight of NrdF2 is 36.9 kDa. Supplementary Fig. 3C shows a 15% SDS gel used to visualize the free NrdI band of 16 kDa, along with free NrdF2 and crosslinked bands. To improve clarity in distinguishing between the crosslinked NrdF2 dimer and the NrdF2 dimer crosslinked with NrdI, the sample was subsequently loaded onto a 10% SDS gel as shown in Supplementary Fig. 3D. Consequently, the NrdF2 band appears with altered mobility compared to its appearance in the gel shown in Supplementary Fig. 3C. This slight change in band position, i.e. lower on a 10% SDS gel can be attributed to the differences in pore size and electrophoretic conditions that may affect the mobility and apparent position of the protein band. Moreover, cross linking experiments also demonstrated stoichiometry of 2:1 (Supplementary Figs. 3C and D). Earlier study done using quantitative

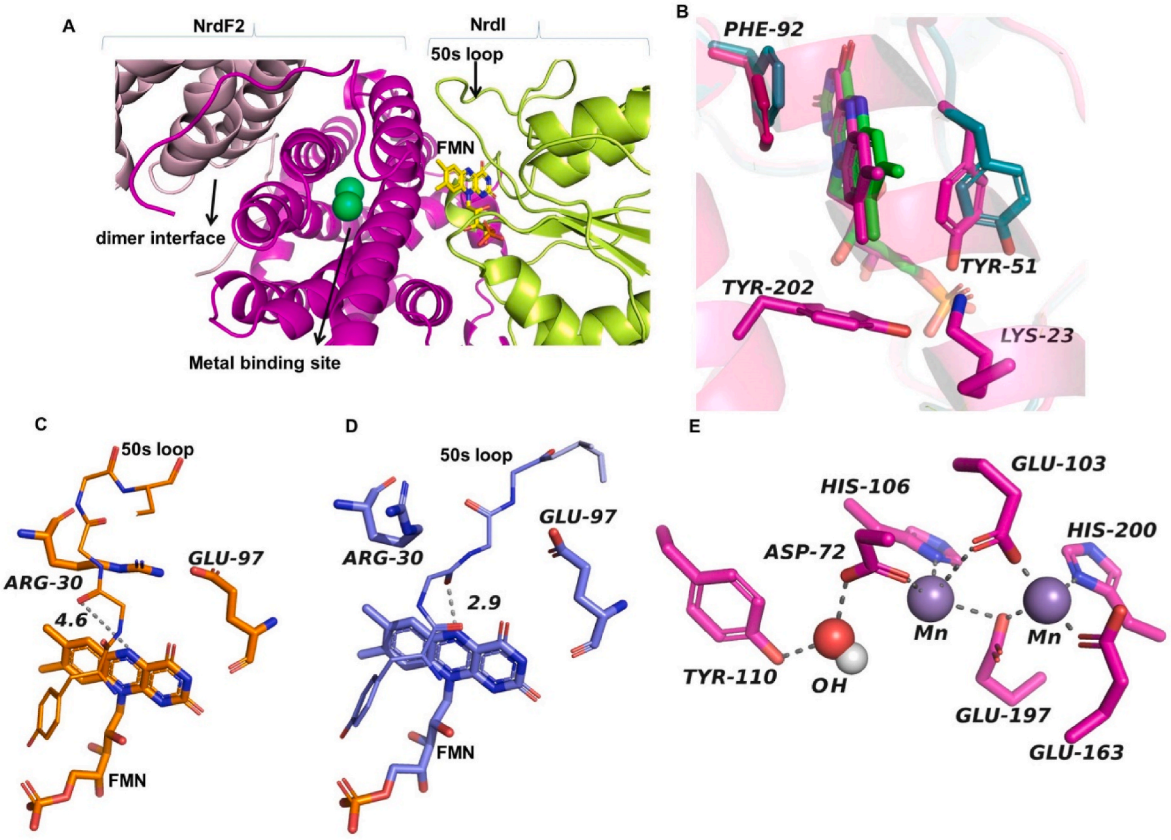

Fig. 2. Interface of complex of Mtb NrdF2I: (A) Interaction of NrdI and NrdF is characterized by close interactions of the radical transfer groups. FMN of NrdI is placed close to the di-manganese binding site so that superoxide radical produced by FMN can be transported to metal centre. 50s loop of NrdI (green) makes association of NrdF2 (pink) and NrdI more intimate. **(B).** Subtle differences in the structures of NrdI and NrdF2I complex. A rotation in NrdI Tyr 51 side chain of complex was observed promoting closer interactions of NrdF2 and NrdI subunits. **(C)** During complex formation among the structural changes is the reorientation of Arg 30 side chain and 50s loop between the oxidised **(D)** and reduced forms **(E)** Residues involved in Mn binding in the NrdF2I complex. (For interpretation of the references to color in this figure legend, the reader is referred to the Web version of this article.)

Western blot had indicated 13 fold lower expression of NrdI than NrdF2 supporting the hypothesis that NrdI may have only catalytic role (Cotruvo and Joanne, 2011) suggesting that our observed stoichiometry might not be an artefact.

2.2.2. Interaction interface of the complex

In the crystal structure of the NrdF2I complex, the association of the two molecules is such that the FMN cofactor of NrdI and di-Manganese atoms of NrdF2 are in close vicinity. Such a placement makes them apparently poised for the superoxide radical transfer (Fig. 2A). The buried surface area between NrdF2 and NrdI in both the oxidised and reduced forms is almost similar, that is ~1000 Å^2 (Evgeny, 2010; Krissinel and Kim, 2005, 2007).

To examine the variation observed in NrdI post complex formation with NrdF2 in the NrdF2I interface, superposition was performed. However structure of the standalone Mtb NrdI protein is not available in literature. Mtb NrdI closely resembles Mth NrdI, sharing 86% sequence identity. Structural superposition of standalone Mth NrdI with Mtb NrdI from the NrdF2I complex shows an RMSD of 0.38 Å. Therefore, standalone Mth NrdI was used to understand the change induced following complex formation. Superposition of Mth NrdI with that of Mtb NrdF2I complex indicated 90° rotation of Tyr 51 of Mtb NrdI (Mth Tyr 49) towards FMN in the complex. The rotation and movement of the Tyr facilitates its intersubunit interaction with Tyr 202 and Lys 23 of NrdF2 and PO3 group of FMN. The interactions of Lys 23 and Tyr 202 with Tyr 51 appear to stabilise the NrdF2 and NrdI interactions in the complex (Fig. 2B).

2.2.3. Comparative analysis of oxidised and reduced Mtb NrdF2I complex

The RMSD of the reported Mtb NrdF2 structure (Uppsten et al., 2004) with our complex structure is 0.35 Å indicating no major structural change in NrdF2 in oxidised and reduced forms. The major change between the reduced form of the complex compared to the oxidised form is at the interface near the NrdI 50s loop. An ionic interaction is observed between NrdF2-Arg 30 and NrdI-Glu 97 in the oxidised but not in the reduced complex. The orientation of NrdF2-Arg 30 in oxidised complex

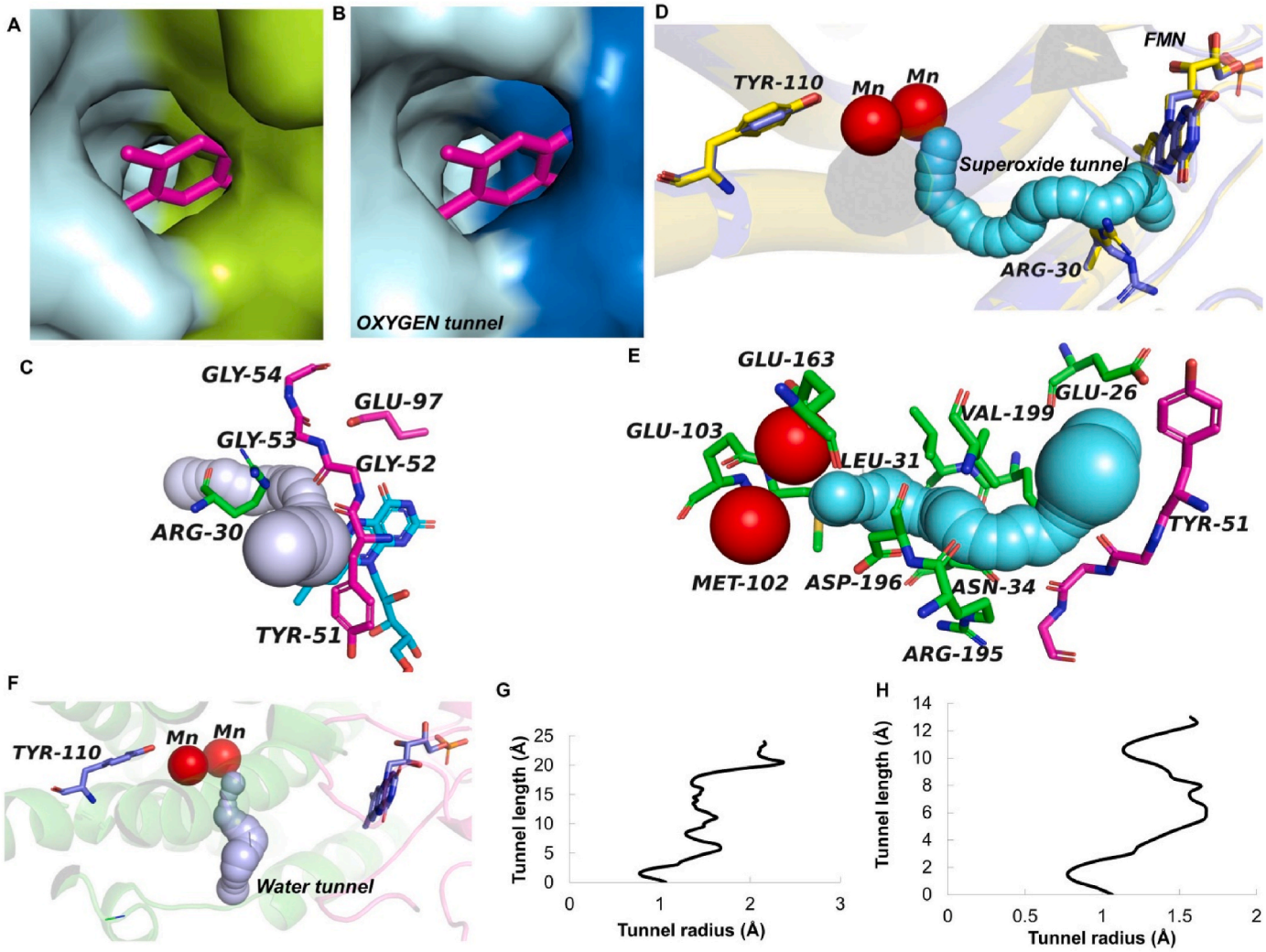

Fig. 3. Channel formation in reduced complex of Mtb NrdF2I: Oxygen tunnel, superoxide tunnel and water tunnel connecting to FMN and metal cofactor site are important in initiation of radical formation and assembly. A prominent tunnel is seen starting from the surface of the NrdI structure and reaching FMN. We believe that this oxygen tunnel is able to carry O_2 to the FMN site in reduced form. The oxygen tunnel is substantially constricted in the oxidised form **(A)** and expanded in the reduced **(B)** structure. **(C)** Residues lining the oxygen tunnel with residues from NrdF2 are shown as green and NrdI as pink. **(D).** Another tunnel starting from FMN in NrdI and reaching the di-manganese site in NrdF2 is present. Formation of this tunnel is seen only in the reduced complex structure, and has been implicated in other similar structures to carry the superoxide to the metal binding site (see text for details). **(E).** Residues lining the superoxide tunnel identified by CAVER. Residues from NrdF2 are shown as green and NrdI as pink. **(F)** Water tunnel to di-manganese site in NrdF2 is present which may play important role in reduction of Mn. Profile of the superoxide tunnel **(G)** and water tunnel **(H)** indicating the radius at different parts of the tunnel. (For interpretation of the references to color in this figure legend, the reader is referred to the Web version of this article.)

occludes interaction of 50s loop with FMN but enables its interaction with FMN in the reduced complex. Consequently, in reduced complex the 50s loop reorients and moves towards NrdI facilitating the hydrogen bonding interaction of carbonyl oxygen of Gly 52 and N5 atom of FMN (Fig. 2C and D).

2.2.4. Tunnels for oxygen and superoxide

In the NrdF2I complex structure, a prominent tunnel is seen in NrdI starting on its surface and reaching up to FMN. Visual inspection indicates that the tunnel is constricted in the oxidised form (Fig. 3A) compared to its reduced structure (Fig. 3B). The tunnel radius of 2.15 Å in the reduced form is adequate for oxygen to enter and reach up to FMN. The residues present in direct contact with the oxygen tunnel are Tyr 51, Arg 30, Gly 52 and 53. The orientation of Gly 53, Tyr 51 and Arg 30 is such that the methyl carbons of the residues line up the oxygen channel giving distinct hydrophobic character to the tunnel (Fig. 3C). Moreover, Gly 52 carbonyl group in reduced form moves inward forming hydrogen bond with N(5) of FMN creating space and environment for oxygen to enter the tunnel. In the reduced form reorientation of Arg-30 of NrdF2 and 50s loop of NrdI away from each other leads to opening of the tunnel (Fig. 2D).

The C4a atom of the isoalloxazine ring of FMN is the site of interaction and reduction of O_2 to superoxide (Beaupre and Moran, 2020). We observe another tunnel in the reduced form of the NrdF2I complex from FMN in NrdI to the dimetal site in NrdF2 (Fig. 3D). The tunnel has been speculated to be the path for superoxide radical transfer to activate Mn site (Boal et al., 2010; Hammerstad et al., 2014). We also observed density in this tunnel which was modelled as superoxide. The superoxide tunnel in our structure does not overlap in position with that reported in earlier structures (Hammerstad et al., 2014; Boal et al., 2010). Of the 29 amino acids that are closer and pointing towards the 16 Å superoxide tunnel are Leu-31, Arg-30, Glu-26, Val-199, Asn-34, Asp-196, Arg-195 from NrdF2 and Phe-94, Glu-97, Tyr-51, Gly 52–54 from NrdI (Fig. 3E). The reorientation of Arg 30 in the reduced complex leads to widening of tunnel gap from 1.5 to 3 Å hence opening up for superoxide radical to pass through the tunnel. Thus, Arg 30 of NrdF2 and the 50s loop of NrdI in unison appear to act as a gate for oxygen and superoxide transport.

Interestingly, a tunnel appears to be present from the surface of NrdF2 structure to the Tyr 110 residue (Fig. 3F). Fig. 3G and H shows the profile of the superoxide tunnel and water tunnel respectively indicating the radius at different parts of the tunnel. Although the tunnel is constricted, with minor movement of residues, the tunnel might be able to carry a water molecule to the site (Fig. 3H).

2.2.5. Metal cofactor site in NrdF2I complex

X-ray fluorescence scan of protein complex crystals indicated characteristic K edge emission of manganese at ~6.5 keV, thus confirming presence of Mn and not Fe (Fig. 4A). To confirm the presence of manganese site at the NrdF2I unambiguously we have performed the X-band cw-EPR measurement. A well-resolved EPR spectrum was observed at g = 1.99 with hyperfine interaction (nuclear spin of manganese $(I_{Mn}) = 5/2$; 100% abundance). This EPR spectral signature confirms the divalent oxidation state of the manganese (high spin S = 5/2). An excellent agreement between the experimental EPR spectrum (Fig. 4B black trace, and simulation red trace) was obtained using the following parameters g = 1.99 Voigtian broadening [2,0.9] mT and A = 268 MHz. Upon exposing the oxidised metal site (Mn^{III} Mn^{IV}) of NrdF2I to an O_2 atmosphere, the manganese ions are reduced back to Mn(II), regenerating the reduced metal site of NrdF2. This results in the reappearance of the EPR

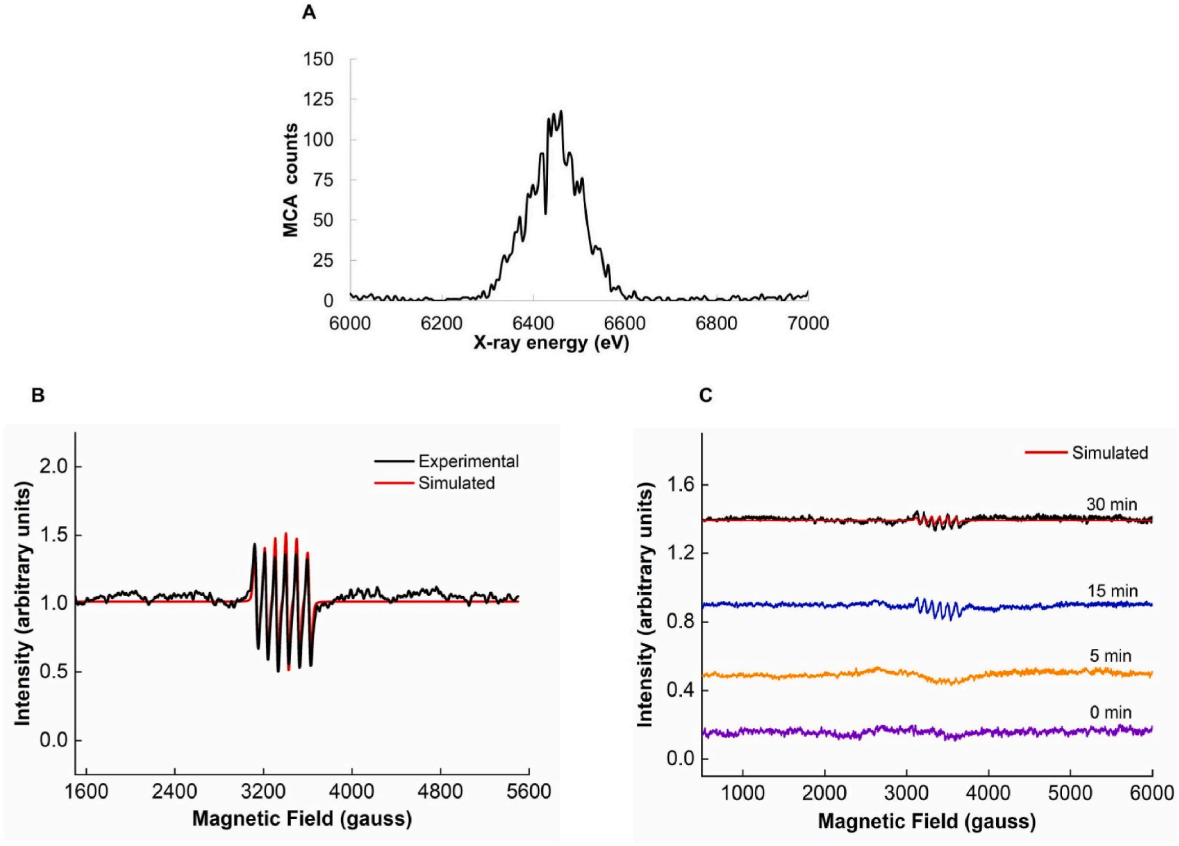

Fig. 4. X-ray Fluorescence scan and CW-EPR spectroscopy: (A). The K edge absorption at 6.5390 keV indicates presence of manganese metal. **(B)**. The X-band CW-EPR spectrum of NrdF2I complex in buffer solution (25 mM Tris pH8 and 150 mM NaCl) at 295 K **(C)** The kinetics of the reduction of manganese in NrdF2I is followed by CW-EPR at 295K at different time intervals of 0, 5, 15, 30 min. Simulated data is represented by red trace while other colors represent experimental data. (For interpretation of the references to color in this figure legend, the reader is referred to the Web version of this article.)

signal at the same position observed in reduced metal site (Fig. 4C).

Residues involved in interaction with metal ions in NrdF2 are His 200, His 106, Glu 163, Glu 103, Glu 197 and Asp 72 (Fig. 2E). The 2 manganese ions are at a Mn - Mn distance of ~3.8 Å. Tyr 110 implicated in free radical formation is placed close to the di-manganese binding site approximately at a distance of 6 Å. Tyr 110 is immersed in a complete hydrophobic environment surrounded by side chains of Phe 65, Ile 190, Ile 193, Phe 171, Leu 68 and Phe 167. Interestingly, Glu-163, which is one of the Mn-coordinating residues, possesses different orientation from the equivalent Glu-158 from *E. coli*. In all other NrdF and NrdFI complex structures, residues equivalent to Glu-163 are in similar orientation as that in the Mtb NrdF2I complex (Fig. 5A). This orientation permits monodentate coordination with Mn ion. On the other hand, in *B. cereus* (4BMU) and *E. coli (3N39)* structures of NrdFI complex, the Glu residue exhibits bidentate interaction with manganese (Hammerstad et al., 2014; Boal et al., 2010) (Fig. 5B and C). Alternate conformations were visible in *B. cereus* structure raising the possibility of both bidentate and monodentate interactions (Fig. 5B).

An interesting observation in our structure is that in ten out of the twelve chains of NrdF2 (oxidised and reduced) there is a strong density between the Mn1 (Mn at site close to Tyr 110) and Tyr 110 at a distance of 2.1–2.2 Å from the side chain hydroxyl of Tyr 110 (Fig. 5D and E). This distance is shorter than the typical range for a hydrogen bond (2.8–3.2 Å), suggesting the potential presence of another type of interaction or molecule, which led us to model a hydroxide group (Fig. 5A) (Minch, 1999).

3. Discussion

Prior studies have shown that in Mtb and other Mycobacteria, Class Ib NrdF2 provides the only and essential ribonucleotide reductase activity, although there are paralogs of NrdF present on the genome (Mowa et al., 2009). Different subunits of RNR, namely NrdE, NrdF2 and NrdI, and the thioredoxin-like protein NrdH therefore offer as attractive drug targets (Phulera and Mande, 2013; Arora et al., 2011). Structural information on these has been limited, and especially the structures of their complexes are not known. In this report we present the crystal structures of NrdI and NrdF2I in oxidised and reduced forms. We have also been able to obtain insights into the complex structures of NrdE, NrdF2 and NrdI through single particle cryo- Electron Microscopy (manuscript in preparation).

Radical formation during ribonucleotide reduction in Class Ib RNRs occurs at the di-metal site in β subunit assisted by superoxide generation at the FMN site in NrdI. It has been reported that β or NrdF subunits of Class Ib RNRs, when expressed heterologously in *E. coli,* are found to contain Manganese (Lofstad et al., 2016). This is unlike the equivalent NrdB subunit of the Class Ia RNR, where Iron is found to bind to NrdB. In our study on NrdF2I complexes, the identity of metal was indeed

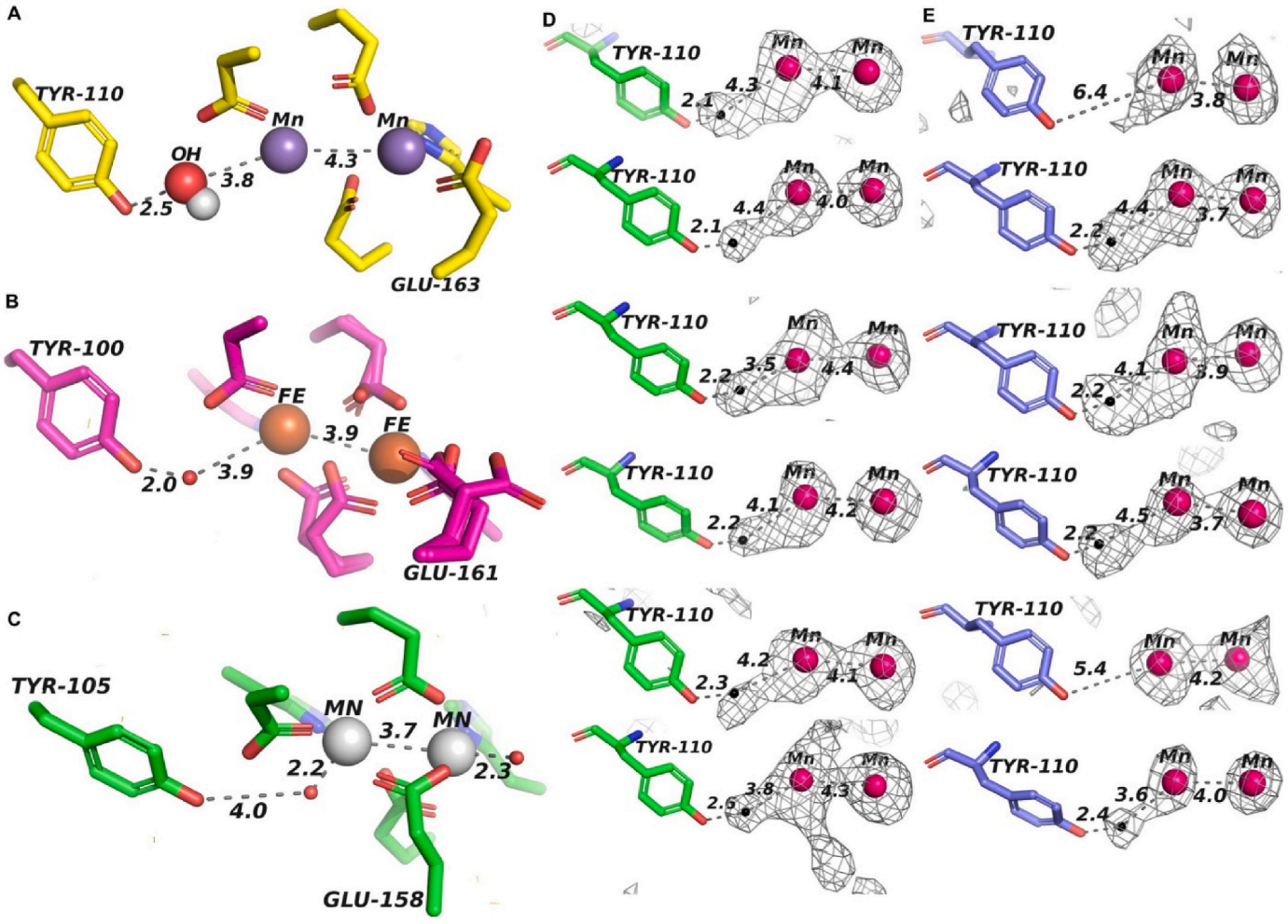

Fig. 5. Geometry of interactions at the metal-binding site: Interaction at the metal site in NrdFI complex structures **(A)** Mtb NrdF2I, **(B)** *B. cereus* **(C).** *E. coli*. The black color sphere indicates water molecules present close to the metal cofactor site. The Fo-Fc difference density map contoured at 3σ from different NrdF2 chains of asymmetric unit in **(D)** oxidised (green) **(E)** reduced (blue) NrdF2I complex structure at metal cofactor (Mn) site. (For interpretation of the references to color in this figure legend, the reader is referred to the Web version of this article.)

observed to be Manganese by X-ray fluorescence scan. Similarly, previous work by Grave et al. also demonstrated preference of manganese over iron in Class 1b RNR of *B. cereus* (Grāve et al., 2020). The two Mn are coordinated, as in other reported structures, by a number of Glu, Asp and His residues (Boal et al., 2010; Hammerstad et al., 2014). The structures of NrdF2I complexes, in oxidised and reduced forms, thus reveal the mechanism of free radical generation in details.

3.1. Unusual stoichiometry of NrdF2: NrdI complex

One of the intriguing observations in our structures relates that to the stoichiometry of the NrdF2I complex. Stoichiometry of the complex as seen in our structure is 2:1 between NrdF2 and NrdI subunits. This is different than observed in other structures, where 1:1 stoichiometry has been reported (Hammerstad et al., 2014; Boal et al., 2010). Our SEC MALS study, glutaraldehyde crosslinking and single particle CryoEM study images appear to reinforce the 2:1 stoichiometry. Further detailed studies will be needed to confirm the same. The subtle difference in activity of 1:1 complex compared to 2:1 stoichiometry can be understood in terms of tyrosyl radical generation. In 1:1 complex, both the subunits of NrdF dimer will be in a position to generate Tyr radical in the respective subunits, whereas in the 2:1 complex, only the subunit of NrdF, which is bound to NrdI, will be in a position to generate a Tyr radical.

The different subunits of RNR involve NrdE (catalytic subunit), NrdF2 (that generates tyrosyl radical at metal site) and NrdI (helps NrdF2 in assembly and maintenance of radical). NrdE and NrdF2 exist as dimers, whereas NrdI exists as a monomer. Interestingly, although NrdEF is a heterotetramer it forms an asymmetric complex. Only one chain of NrdE interacts with one chain of NrdF, and is thereby poised to receive free radical from interacting NrdF partner (Uppsten et al., 2006; Kang et al., 2020). Thus, there is need for forming Tyr radical in only one subunit of NrdF. The 2:1 stoichiometry of NrdF2:NrdI, when viewed in the context of asymmetric NrdEF complex appears to be justified (Uppsten et al., 2006; Kang et al., 2020). If the stoichiometry of NrdF: NrdI were 1:1, free radical would have formed in both the subunits of NrdF simultaneously, whereas only one NrdF subunit would transfer the free radical to NrdE in the NrdE:NrdF complex. We therefore believe that simultaneous formation of free radical in both the NrdF monomers facilitated by NrdI might not be required. This extra tyrosyl radical formed in other subunit of NrdF2 not associated with NrdE may lead to diffusion of radical. However, binding of one NrdI subunit to one chain of NrdF2 in dimer and how it precludes binding of another NrdI molecule in order to have stoichiometry of 2:1 is not clear.

3.2. Channel accessible to FMN and from FMN to metal cofactor site in NrdF2

One of the hitherto unknown features of the NrdF2I complex has been the mode of entry of oxygen to the FMN site. Our observation of a tunnel with a clear access to FMN explains this elegantly. The tunnel is seen to be wide enough to carry an oxygen molecule when NrdI is in the reduced form. Moreover, the tunnel has distinct hydrophobic character to allow entry of molecular oxygen as mentioned earlier. Ionic interaction between Arg 30 of NrdF2 and Glu 97 of NrdI appear to control gating mechanism of the channel. The glutamate arginine pair residues in FAD containing cholesterol oxidase (Coulombe et al., 2001) is similar in regulating oxygen access and other residues involved in path of oxygen transfer (Romero et al., 2018). It is well known that a fully reduced FMN can transfer electron to O_2 to form a superoxide radical (Pryde and Hirst, 2011; Kussmaul and Hirst, 2006). We propose that as soon as oxygen is converted into a superoxide radical and NrdI is oxidised, NrdF2 Arg 30 side chain and NrdI 50s loop move towards each other constricting the channel and setting the stage for the superoxide radical for further transition to the di-metal site in NrdF2 structure (Fig. 2C and D). We believe that the oxidation-reduction process modulates the access of oxygen at this site such that only reduced FMN would be able to receive oxygen for the subsequent cycle of superoxide radical generation. Examination of NrdFI structures from *E. coli*, *B. cereus* and *A urinae* exhibit a similar oxygen tunnel like Mtb NrdF2I (Supplementary Fig. 5 A-E upper panel). Despite this, variations in amino acid residues are observed (Supplementary Fig. 5 F-J lower panel): *E. coli* has an arginine: alanine pair, while *B. cereus* has a glutamine:lysine pair at this specific position. Class 1e *Aerococcus. urinae* has arginine and serine pair present near the oxygen tunnel. Multiple sequence alignment shows Arginine (58%) is conserved at this position with lysine (21%) and Glutamine (18%) present in some of the cases. These differences in amino acid composition can potentially influence the properties of the tunnel which may impact substrate binding or diffusion rates. In Mtb, a glutamate: arginine pair may regulate tunnel size, potentially preventing superoxide radical diffusion, crucial for survival in oxygen-deficient conditions. The regulation in Mtb through glutamate:arginine pair and long 50s loop may likely represent a mechanism of adaptation of Mtb in its host environment, where the bacterium must effectively manage reductive stress while thriving in low-oxygen conditions.

Another tunnel between the FMN binding site of NrdI and di-Manganese binding site of NrdF2 is observed in the reduced NrdF2I complex. Formation of this tunnel is facilitated by subtle structural changes that occur at the interface of the NrdI and NrdF2 subunits. Prominent among these is the flip of NrdF2 Arg 30 side chain, which is involved in intersubunit hydrogen bond in the oxidised complex, but it flips away from the interface in the reduced form. NrdF2 Arg 30 thereby appears to play an essential role in gating entry of oxygen in reduced form and gating diffusion of superoxide radical in the oxidised form (Supplementary Figs. 5I and J). Observation of similar kind of tunnel has been reported in other structures and has been speculated to carry the superoxide radical from the FMN to the di-Manganese site (Boal et al., 2010; Hammerstad et al., 2014). The position of the tunnel of superoxide radical transfer in Mtb is different than observed in *E. coli* and *B. cereus* structures suggesting possible presence of alternate route for superoxide transfer. Study by Wang et al. through multiscale molecular simulation approach had similar observation in which diverse networks exist for H_2 and O_2 gas molecules reach the active site in the [NiFe]-Hydrogenase (Wang et al., 2011). Additionally *B. anthracis* $NrdF_{(semiox)}$-NrdI model proposed a mechanism to prevent premature loss of the superoxide and stop the injection of a second superoxide species which would likely rapidly quench the tyrosyl radical (Grāve et al., 2019). The model structure highlight how rearrangement of metal and metal-coordinating residues affects Tyr 166 in the αE segment, facilitating a polar interaction with the αF segment of NrdF2, ultimately sealing the superoxide channel (Grāve et al., 2019). Involvement of different residues in modulating activity of these tunnels can be confirmed by mutational studies, which we believe will provide a strong evidence for this mechanism.

3.3. The role of Mn^{III} Mn^{IV} in Tyr• radical formation

It is well-documented that the superoxide radical anion ($O_2^{\bullet-}$) generated upon activation of O_2 by the reduced FMN site, eventually oxidizes the divalent Mn(II) sites at NrdF2I via the superoxide tunnel (Cotruvo et al., 2013; Doyle et al., 2024). To provide indirect evidence for this process, we reduced the FMN site using an excess of sodium dithionite under aerobic conditions. The formation of Mn(III), an integer spin coupled with Jahn-Teller distortion, often leads to a large zero-field splitting, rendering this ion EPR silent. Similarly, the inherent fast relaxation of the spin associated with Mn(IV) at higher temperatures also makes this species EPR silent at room temperature. In line with this observation the well-resolved EPR spectral signature previously observed in reduced metal site (Fig. 4B) of NrdF2I completely disappears in oxidised metal site (Fig. 4C) indicating the following sequence of reactions: (i) reduction of FMN by dithionite results in the reduction of O_2 to superoxide radical, (ii) the superoxide radical reaches the NrdF2

sites through the tunnel and oxidizes Mn(II) to higher oxidation states (Mn(III) and/or Mn(IV)) (Doyle et al., 2024). (iii) The transient Mn^{III} Mn^{IV} attack Tyr 110 and abstracts electron. Subsequently through a proton coupled electron transfer form the Tyr• radical. However, we could not detect signals attributed to tyrosine radical formation under our experimental conditions. This absence could be due to the transient nature of the radical, radical quenching or its high reactivity. However UV–visible spectroscopy performed in presence of sodium dithionite showed peak at 410 nm signature of tyrosyl radical (data not shown). The formation of this (410 nm) band coupled with the disappearance Mn (II) signals upon oxidation indicates the mechanism of formation of tyrosine radicals in the β subunit of the ribonucleotide reductase complex in *M. tuberculosis.*

To prove further the importance of FMN site for the oxidation/reduction of the metal sites at NrdF2I we have performed an EPR kinetics studies. As stated earlier, the EPR signal of Mn(II) disappears upon oxidation of the metal sites at NrdF2I (due to superoxide radical formation via reduction of O2 by the reduced FMN). Upon exposing the oxidised metal site of NrdF2I to an O_2 atmosphere, the manganese ions are reduced back to Mn(II), regenerating the reduced metal site of NrdF2I. This results in the reappearance of the EPR signal at the same position observed in the native NrdF2I (Fig. 4C). This evidently emphasizes the involvement of FMN subunit for the oxidation/reduction of Mn(II) ions at the NrdF2I.

A high resolution data of *C. ammoniagenes* R2F structure indicates a hydroxo/water group (O3) coordinated to Mn is present at a distance of 5.6 Å from the Tyrosine (Y115) (Cox et al., 2010). Intriguingly in our structures we did not find any water molecule in the vicinity of the di-manganese binding site, but rather we found presence of density in ten out of twelve chains of NrdF2 close to Tyr 110 residue (Fig. 5D and E). This density is at a very short distance from Tyr-OH, i.e. 2.1–2.2 Å, too short to form a hydrogen bond with a water molecule. A similar density, interpreted as a water molecule at a distance of 2.0 Å, is also observed in the high-resolution (1.8 Å) structure of *Bacillus cereus* (Fig. 5B). This density in Mtb NrdF2I and *Bacillus* structure is present at a distance even lower than low-barrier hydrogen bonds (Kaledhonkar et al., 2013). We believe that this density might correspond to an uncharged hydroxide ion, and not water. The OH-Asp 72 distance of ~2.8 Å indicates that it an uncharged OH• which otherwise would have resulted in repulsion. A similar kind of short O•••O bonds in the X-ray free electron laser structures of the photosystem II was observed. The quantum mechanical/molecular mechanical approach suggested presence of the $OH^{\bullet}$ formation between O4 of catalytic centre and a water at a distance <2.3 Å (Mandal et al., 2021). We therefore hypothesise that the distance of 2.1 Å is indicative of presence of hydroxyl ($OH^{\bullet}$) which is formed after proton transfer (Fig. 5D and E). In class Ia RNR, Mössbauer spectrum and density functional theory calculations of diferric cluster similarly indicate deprotonation of the Fe1-coordinated water ligand to yield the neutral Tyrosine (Wörsdörfer et al., 2013). Thus, the extended density observed between Mn1 and Tyr 110 at a distance of 2.1 Å may signify an intermediary step between radical translocation and the resting phase.

If indeed this is the case, this observation would strongly indicate the mechanism of Tyr• formation. The redox potential and pKa of the groups involved for such a radical formation reaction might be modulated by the strongly hydrophobic environment of this site.

3.4. Intermediates states of metal cofactor site assembly

Mn metal cofactor might undertake multiple intermediate states to generate Tyrosyl radical post oxidation by superoxide. The Mtb NrdF2I structures in oxidised and reduced forms, along with NrdFI structures of *E. coli*, *B. cereus* and other NrdF structures might indicate some of the stages of metal cofactor assembly in Tyrosyl radical generation (Fig. 5A, B, C). The different metal oxidation states observed in these structures are presumably different metal cofactor assembly intermediates formed in the process of Tyrosyl radical generation.

In the NrdF apo structure the metal-binding site configuration is maintained despite the absence of metal ion through a network of hydrogen bond and a water molecule (Grāve et al., 2019). Whereas in the holo structures different number of water molecules coordinate the dimetal site indicating that they may play important roles in cofactor assembly and maintenance. The binding of water molecule to the cofactor site may keep the cofactor assembly stable and dissociation of it may allow oxidant to bind to the metal ion as observed in Mn catalases (Barynin et al., 2001). Interaction of the metal with water also assists in ionisation of the metal ion through hydration energy.

In the reported structures of the oxidised form, the metal ions are closer and they coordinate with water molecule poised to attack the Tyr (Cox et al., 2010; Grāve et al., 2019). However, the distance between Mn1 and Mn2 as observed in our structures is between 3.7 and 4.2 Å, but without the oxobridge, which is reminiscent of structures reported (Grāve et al., 2019). Therefore, the observed metal cofactor state in our NrdF2I structures may be imagined as those of an intermediate step between the Mn coordinated oxobridge form and Tyrosyl radical formation state.

Once the Mn1 and Mn2 are oxidised by the superoxide radical, the next step would be the formation of Tyr radical. Our data suggests evidence for this. Previous report on mechanism of Tyrosyl radical generation utilising dinuclear Iron Cluster using stopped-flow absorption and rapid freeze-quench EPR spectroscopy demonstrated two types of intermediates a μ-peroxodiferric complex (named as U) and an iron-coupled radical (named as X) involved in Tyrosine oxidation (Bollinger et al., 1991). Rapid freeze-quench Mössbauer spectroscopy indicated that intermediate X is a free radical derived from oxygen or protein. Further study by Worsdorfer et al. indicated water coordinated with Fe1 serves as proton coupling partner to Tyrosine and has direct role in catalysis (Wörsdörfer et al., 2013). Extraction of proton from water by Tyr 110 results in presence of OH group close to Tyrosine. We propose that the extended density we observe between Tyr110 and Mn1 could be equivalent to intermediate X (Bollinger et al., 1991) or radical-translocation-product state (Wörsdörfer et al., 2013) where water in vicinity of metal ion has transferred the proton to Tyrosine. Moreover, the distances of Tyr 110 to Mn1-coordinating Asp (Mtb 72, *E. coli* 67 and *B.* cereus 62) are 4 Å, 2.7 Å and 3.4 Å respectively. Similarly, the distances between the Asp and Mn vary from 1.8 Å to 2.4 Å. This conformational variation suggests the role of Asp in generation of MnIII 2-Y• cofactor. EPR analysis also indicates that MnIII 2-Y• is an active cofactor (Cotruvo et al., 2013; Joseph A. Cotruvo Jr and JoAnne Stubbe, 2008). Thus, it can be hypothesized that interaction of the Mn through hydroxide with Tyr proceeds with radical transfer.

Single-crystal high-field EPR and X ray data analysis reveal rotation of Y122● radical side chain away from the metal site compared to reduced Tyrosine-OH (Högbom et al., 2003). Orientation of Tyrosine in *E. coli* and *B. cereus structures* is almost equivalent to the state where Tyrosine is in reduced state. Our structure is similar to where tyrosyl radical is formed and Tyrosine side chain has moved away from the metal centre and poised for radical transfer (Fig. 6D). Similarly, the movement of Tyrosine away from metal cofactor site may provide access to water to enter at the dimetal site and eventually bring about protonation of this metastable state (Mn1–OH) to stable (Mn1-OH_2/Y) water associated state. Thus, position of Tyrosine side chain in Mtb represents its state after radical formation.

Thus, a channel in the reduced NrdF2I structure for carrying oxygen from surface of the molecule to the FMN site, another channel to carry superoxide from the FMN in NrdI to di-Manganese site in NrdF2, disorder in the Mn1-binding and its association with Tyr 110 via hydroxide ion, and a water channel to the Tyr 110 of NrdF2 would complete the structural view of radical generation in the Class Ib RNR family. An animation capturing these steps is depicted in Supplementary Video 1. Fig. 6 depicts a brief comprehensive overview of oxygen entry to radical transfer from Tyrosine and reduction of Tyrosine aimed at forward

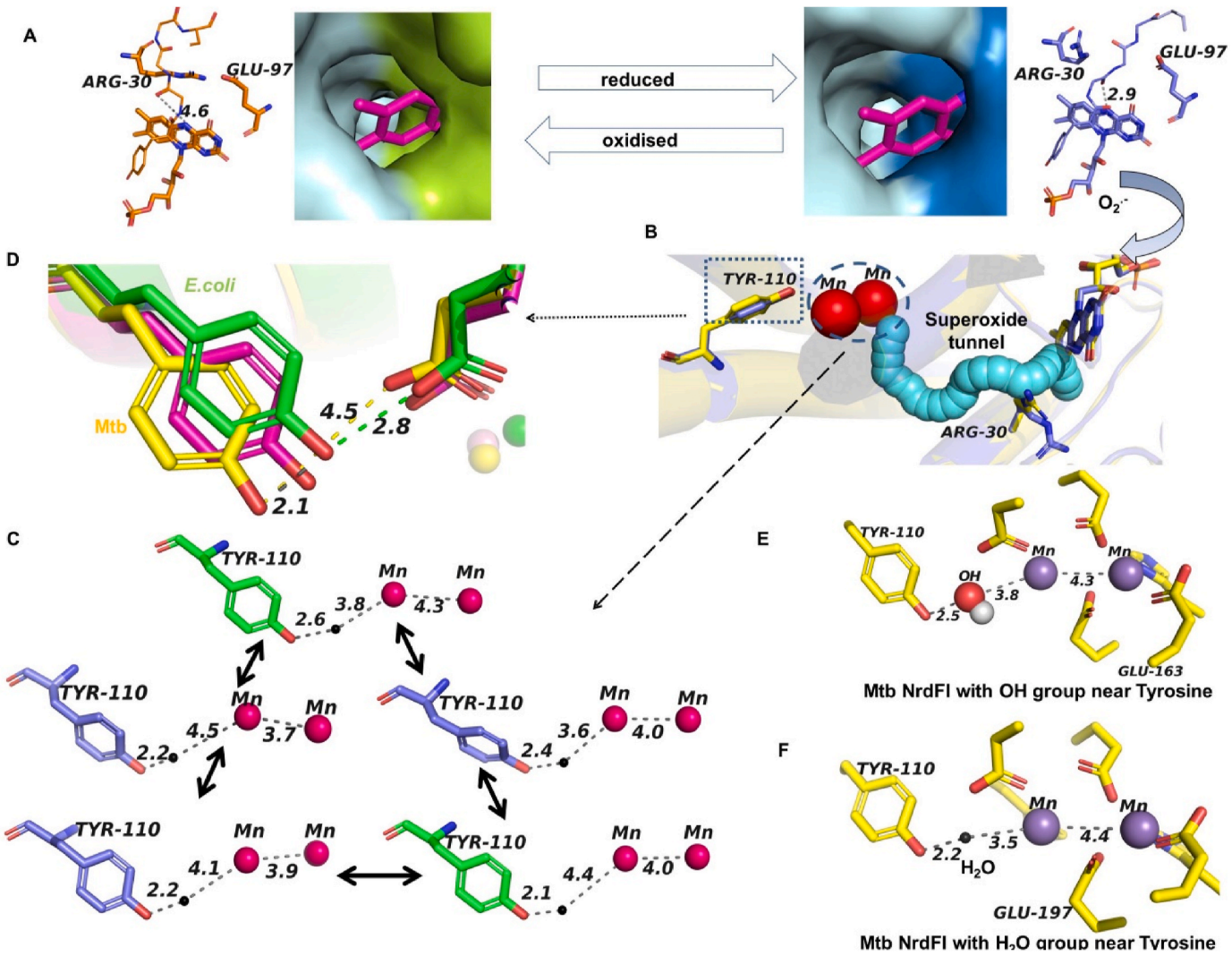

Fig. 6. Detailed overview and structural insights into initiation of free radical mechanism and generation of tyrosyl radical:
Comparative analysis with previous and current work offers a detailed overview and structural insights into initiation of free radical mechanism and generation of tyrosyl radical. **(A)** shows tunnel at the NrdFI interaction interface with a clear access of oxygen to FMN. Our structure shows that the tunnel is wide and hydrophobic enough to carry an oxygen molecule when NrdI is in the reduced form. The Glutamate and Arginine pair interaction control gating mechanism of this oxygen tunnel. **(B)** shows the superoxide radical formed at the FMN site is transferred through superoxide tunnel to metal cofactor site leading to Mn oxidation. **(C)** The MnIII-MnIV intermediate formed after oxidation from superoxide radical oxidizes Tyrosine leading to tyrosyl radical generation. Along with other residues the metal cofactor site is coordinated with water molecule. The density for this coordinated water molecule is present in *E. coli* NrdFI structure (Fig. 3C). This water has role to play in hydrogen bond formation between redox active Tyrosine and metal site via aspartic acid. The Mn1-Mn2, Mn1-OH_2, Tyr-OH_2 and Tyr-OH distance in different NrdF2 chains in our reduced and oxidised structure give a clue to different intermediate steps that NrdF2 engage in to facilitate forward radical translocation and reverse radical translocation. The different chain of NrdF2 of Mtb NrdF2I complex in oxidised and reduced form has presence of density modelled as water near Tyrosine at a variable distance of 2.1 to 2.6 Å which may depict different forward and reverse radical translocation phase. **(D)** The tyrosyl radical formed upon oxidation, flips away from metal site. The flipped Tyrosine moves closer to tryptophan W36 subsequently oxidising Y305. Movement of Mtb Tyr110 2.1 Å away from metal site compared to *E. coli* indicates towards oxidised Tyrosine formation (M.tb (yellow) *E. coli* (green) and *B. cereus* (pink). The structure of *E. coli* (green) is closer to the resting phase where water is coordinated to the metal site and redox Tyrosine is present closer to the metal site (Fig. 3C). Whereas in *B. cereus* (pink) redox Tyrosine is closer to metal site but density modelled as water is close to Tyrosine at 2 Å which indicates towards the initial steps of forward radical translocation. The forward radical translocation proceeds with reduction of Tyr• radical which require proton transfer to yield reduced Tyrosine. Our structure highlights this step where Tyrosine is reduced and after obtaining proton from water will eventually move towards metal cofactor site. The Mn1–OH formed after proton transfer will eventually be protonated for stabilisation. One possibility of abstracting proton from FMN all the way to Mn1–OH also needs to be considered through a chain of salt bridges involving NrdI Glu 96 and NrdF2 Arg 95, Asp 196 and His 106. **(E)** Since post proton transfer OH radical will remain on metal site we have modelled OH group near Tyrosine. **(F)** When water is modelled near Tyrosine its leads to a short contact with Tyrosine. (For interpretation of the references to color in this figure legend, the reader is referred to the Web version of this article.)

radical translocation. Molecular simulations and a higher resolution view of the structures will further assist in understanding of these steps. Understanding the tunnels and gating mechanism not only provide information of functioning of protein but also can be targeted for pharmacological or therapeutics purposes in general. Cystic Fibrosis (Linsdell, 2017), Epilepsy (Nilsson et al., 2022), Bartter Syndrome, potassium channel (Li et al., 2023) are few of the examples that highlight the critical role of protein tunnels and gating mechanisms in normal physiological processes. Blocking or modulating these tunnels can alter protein activity, potentially offering therapeutic benefits. *Mycobacterium tuberculosis* RNR (class 1b) utilizes manganese in NrdF2, assisted by NrdI for tyrosyl radical generation. In contrast, human RNR

(class 1a) uses iron directly, independent of NrdI due to its ability to interact with atmospheric oxygen. Targeting Mtb RNR takes advantage of these differences, enabling selective inhibition of essential function thereby minimizing side effects

4. Materials and methods

4.1. Purification and crystallisation of different subunit of RNR

E. coli bacterial strain *Origami 2(DE3)* was used for large scale expression and purification of NrdI from Mth NrdF2I (pET28a+/kanr-NrdF2 and Camr His-MBP NrdI) construct. *BL21 (DE3)* strain was used for co-purification of Mtb NrdF2I complex (His-NrdF2-ampr and His-MBP-NrdI-camr). The detailed protocol for purification is discussed in supplementary.

Crystals of NrdI were grown in mother liquor containing 0.15M potassium phosphate monobasic and 18% PEG 3350. Crystals of NrdF2I were grown in buffer containing 0.1M MES pH 6, 1.4M NaCl, 0.075M sodium phosphate monobasic, 0.075M potassium phosphate monobasic. To determine the structure in reduced form, the NrdI and NrdF2I crystals were soaked in 800 mM sodium dithionite in mother liquor till the yellow color of NrdI crystals disappeared.

4.2. Structure solution refinement

Data reduction and scaling for both oxidised and reduced Mth NrdI and Mtb NrdF2I complex were performed using iMOSFLM in CCP4i (Battye et al., 2011). The coordinates of PDB ID 1UZR and PDB ID 3N39 were selected and sequence modified in chainsaw and were then used for molecular replacement in PHASER(McCoy et al., 2007). The co-ordinates of PDB ID 1UZR and PDB ID 3N39 were selected and sequence modified in chainsaw and were then used for molecular replacement in PHASER (McCoy et al., 2007). Model building was performed in COOT (Emsley and Cowtan, 2004) and refined using REFMAC5(Murshudov et al., 2011) and phenix refine(Afonine et al., 2012).

For NrdI reduced, multiple data collected were merged using Blend program (Foadi et al., 2013). For NrdF2I complex, molecular replacement using PDB ID 1UZR identified 6 chains of NrdF2 in asymmetric unit. Fo-Fc density were evaluated and two molecules of NrdI was placed in the asymmetric unit by superposition of NrdF2I (PDB ID 3N39) complex structure of *E. coli* followed by fitting and rigid body refinement. Structure validations of the coordinates were performed using MolProbity (Chen et al., 2010). PyMOL (DeLano WL (2020) The PyMOL Molecular Graphics System, Version 1.2r3pre, Schrödinger, LLC.), Coot (Emsley and Cowtan, 2004) and Chimera (Pettersen et al., 2004) were used for visual analysis and figure preparations.

4.3. Tunnel analysis

CAVER 3.0 PyMOL plugin was used for analysis and visualization of tunnels in NrdF2I complex (Chovancova et al., 2012). 0.7 Å minimum probe radius, 4 and 3 shell depth and shell radius respectively were parameters used for tunnel analysis. Tunnel radius versus tunnel length were plotted to determine the minimum bottleneck radius. Cavity detection radius of 7 Å and cavity detection cutoff of 3 solvent radii in PyMOL were used to analyse the oxygen tunnel in both oxidised and reduced NrdF2I complex.

4.4. PDB ID

The coordinates of Mth NrdI in reduced and oxidised form are deposited in protein data bank under PDB ID 8J4W and PDB ID 8J4V respectively. Mtb NrdF2I complex coordinates are deposited in reduced and oxidised form in protein data bank under PDB ID 8J4Y and 8J4X respectively.

CRediT authorship contribution statement

Lumbini R. Yadav: Conceptualization, Formal analysis, Investigation, Methodology, Validation, Visualization, Writing. **Vasudha Sharma:** helped with data acquisition, analysis, and, writing of EPR data. **Maheswaran Shanmugam:** helped with data acquisition, analysis, and, writing of EPR data. **Shekhar C. Mande:** Conceptualization, Methodology, Project administration, Funding acquisition, Writing.

Declaration of competing interest

The authors declare that they have no known competing financial interests or personal relationships that could have appeared to influence the work reported in this paper.

Data availability

Data will be made available on request.

Acknowledgements

This work was supported by DST/ICD/BRICS/PilotCall2/MRP-TB (G), DST-NPDF (PDF/2015/000961) and DBT-Centre of Excellence Grant (BT/PR15450/COE/34/46/2016), Ministry of Science and Technology, India. IISER-Pune and TMC-ACTREC, India Diffraction Facility for cryooptimisation and initial screening of crystals are gratefully acknowledged. Special thanks to Dr. Gayathri Pananghat (IISER-PUNE) for her useful inputs in structure determination. European Synchrotron Radiation Facility (ESRF ID23), France and Diamond Light Source, UK for X-ray diffraction data collection are gratefully acknowledged. Raghurama P Hegde XRD2 beamline - Elettra Sincrotrone Trieste, Italy is gratefully acknowledged for X-ray fluorescence scan. MS would like to acknowledge the funding agencies SERB (CRG/2023/002178; SPR/2019/001145), CSIR (01(2933)/18/EMR-II), BRNS (58/14-2023-BRNS-37029), IISc-STARs (MoE-STARS/STARS-2/2023–0158), RIFC, EPR central facility, IIT Bombay, India for the financial support. The genomic DNA of M. tuberculosis was a generous gift from Dr. Sharmistha Banerjee, University of Hyderabad-India and M. thermoresistibile was a generous gift from Dr. Christoph Grunder, University of Washington, United States. SCM thanks Anand Deshpande for a generous philanthropic grant to the Savitribai Phule Pune University.

Appendix A. Supplementary data

Supplementary data to this article can be found online at https://doi.org/10.1016/j.crstbi.2024.100157.

References

Afonine, Pavel V., et al., 2012. Towards automated crystallographic structure refinement with Phenix.Refine. Acta Crystallogr. Sect. D Biol. Crystallogr. 68 (4), 352–367.
Ali, Ibrahim, et al., 2022. A comparative DFT study on the π-π stacking interaction of some N-based organic fused heterocycles with eclipsed and staggered conformations. J. Indian Chem. Soc. 99 (10), 100698.
Arora, Ashish, et al., 2011. Structural biology of Mycobacterium tuberculosis proteins: the Indian efforts. Tuberculosis 91 (5), 456–468.
Asmund Kjendseth Røhr, Hans-Petter Hersleth, Kristoffer Andersson, K., 2010. Tracking Flavin Conformations in Protein Crystal Structures with with Raman Spectroscopy and QM/MM Calculations, 49, pp. 2324–2327.
Barynin, Vladimir V., et al., 2001. Crystal structure of manganese catalase from lactobacillus plantarum. Structure 9 (8), 725–738.
Battye, T. Geoff G., et al., 2011. IMOSFLM: a new graphical interface for diffraction-image processing with mosflm. Acta Crystallogr. Sect. D Biol. Crystallogr. 67 (Pt 4), 271.
Beaupre, Brett A., Moran, Graham R., 2020. N5 is the new C4a: biochemical functionalization of reduced flavins at the N5 position. Front. Mol. Biosci. 7.
Boal, Amie K., Stubbe, Joanne, Rosenzweig, Amy C., 2010. Structural basis for activation of class Ib ribonucleotide reductase. Science 329 (September), 1526–1530.
Bollinger, J.M., Edmondson, J.D.E., Huynh, B.H., Filley, J., Norton, J.R., Stubbe, J., 1991. Mechanism of assembly of the tyrosyl radical-dinuclear iron cluster cofactor of ribonucleotide reductase. Science 253 (6), 292–298.

Brignole, Edward J., et al., 2018. 3.3-Å resolution cryo-EM structure of human ribonucleotide reductase with substrate and allosteric regulators bound. Elife 7.
Chen, Vincent B., et al., 2010. MolProbity: all-atom structure validation for macromolecular crystallography. Acta Crystallogr. Sect. D Biol. Crystallogr. 66 (Pt 1), 12.
Chovancova, Eva, et al., 2012. Caver 3.0: a tool for the analysis of transport pathways in dynamic protein structures. PLoS Comput. Biol. 8 (10), 1.
Cotruvo, Joseph A., Joanne, Stubbe, 2008. NrdI, a flavodoxin involved in maintenance of the diferric-tyrosyl radical cofactor in Escherichia coli class Ib ribonucleotide reductase. Proc. Natl. Acad. Sci. U.S.A. 105 (38), 14383–14388.
Cotruvo Jr., Joseph A., JoAnne, Stubbe, 2008. An active dimanganese(III)-Tyrosyl radical cofactor in Escherichia coli class Ib ribonucleotide reductase. Biochemistry 23 (1), 1–7.
Cotruvo, Joseph A., Joanne, Stubbe, 2011. Escherichia coli class Ib ribonucleotide reductase contains a dimanganese(III)-Tyrosyl radical cofactor in vivo. Biochemistry 50 (10), 1672–1681.
Cotruvo, Joseph A., Stich, Troy A., David Britt, R., Stubbe, Joanne, 2013. Mechanism of assembly of the dimanganese-tyrosyl radical cofactor of class Ib ribonucleotide reductase: enzymatic generation of superoxide is required for tyrosine oxidation via a Mn(III)Mn(IV) intermediate. J. Am. Chem. Soc. 135 (10), 4027–4039.
Coulombe, René, Yue, Kimberley Q., Ghisla, Sandro, Alice, Vrielink, 2001. Oxygen access to the active site of cholesterol oxidase through a narrow channel is gated by an Arg-Glu pair. J. Biol. Chem. 276 (32), 30435–30441.
Cox, Nicholas, et al., 2010. A Tyrosyl - Dimanganese Coupled Spin System Is the Native Metalloradical Cofactor of the R2F Subunit of the Ribonucleotide Reductase of Corynebacterium Ammoniagenes, pp. 11197–11213, 12.
Doyle, Lorna, et al., 2024. Class Ib ribonucleotide reductases: activation of a peroxido-MnIIMnIII to generate a reactive Oxo-MnIIIMnIV oxidant. Inorg. Chem. 63 (4).
Emsley, Paul, Cowtan, Kevin, 2004. Coot: model-building tools for molecular Graphics. Acta Crystallogr. Sect. D Biol. Crystallogr. 60 (12), 2126–2132. //scripts.iucr.org/cgi-bin/paper?ba5070. (Accessed 5 April 2023).
Eriksson, Mathias, et al., 1997. Binding of allosteric effectors to ribonucleotide reductase protein R1: reduction of active-site cysteines promotes substrate binding. Structure 5 (8), 1077–1092.
Eriksson, Mathias, Albert, Jordan, Hans, Eklund, 1998. Structure of Salmonella typhimurium NrdF ribonucleotide reductase in its oxidized and reduced forms. Biochemistry 2960 (98), 13359–13369.
Evgeny, Krissinel, 2010. Crystal contacts as nature's docking solutions. J. Comput. Chem. 31 (1), 133–143.
Foadi, James, et al., 2013. Clustering procedures for the optimal selection of data sets from multiple crystals in macromolecular crystallography. Acta Crystallogr. Sect. D Biol. Crystallogr. 69 (Pt 8), 1617–1632.
Grāve, Kristīne, et al., 2019. Redox-induced structural changes in the di-iron and di-manganese forms of Bacillus anthracis ribonucleotide reductase subunit NrdF suggest a mechanism for gating of radical access. J. Biol. Inorg. Chem. 24 (6), 849–861.
Grāve, Kristīne, et al., 2020. The Bacillus anthracis class Ib ribonucleotide reductase subunit NrdF intrinsically selects manganese over iron. J. Biol. Inorg. Chem. 25 (4), 571–582.
Hammerstad, Marta, et al., 2014. Crystal structure of Bacillus cereus class Ib ribonucleotide reductase di-iron NrdF in complex with NrdI. ACS Chem. Biol. 9 (2), 526–537.
Högbom, Martin, Huque, Yasmin, Sjöberg, Britt Marie, Nordlund, Pär, 2002. Crystal structure of the di-iron/radical protein of ribonucleotide reductase from corynebacterium ammoniagenes. Biochemistry 41 (4), 1381–1389.
Högbom, Martin, et al., 2003. Displacement of the tyrosyl radical cofactor in ribonucleotide reductase obtained by single-crystal high-field EPR and 1.4-å x-ray data. Proc. Natl. Acad. Sci. U.S.A. 100 (6), 3209–3214.
Johansson, Renzo, et al., 2010. High-resolution crystal structures of the flavoprotein NrdI in oxidized and reduced states - an unusual flavodoxin: structural biology. FEBS J. 277 (20), 4265–4277.
John, Juliane, et al., 2022. Redox-controlled reorganization and flavin strain within the ribonucleotide reductase R2b–NrdI complex monitored by serial femtosecond crystallography. Elife 11, 1–23.
Jordan, A., Reichard, P., 2003. Ribonucleotide reductases. Annu. Rev. Biochem. 67, 71–98.
Kaledhonkar, Sandip, et al., 2013. Strong ionic hydrogen bonding causes a spectral isotope effect in photoactive yellow protein. Biophys. J. 105 (11), 2577–2585.
Kang, Gyunghoon, Taguchi, Alexander T., Stubbe, Jo Anne, Drennan, Catherine L., 2020. Structure of a trapped radical transfer pathway within a ribonucleotide reductase holocomplex. Science 368 (6489), 424–427.
Krissinel, Evgeny, Kim, Henrick, 2005. Detection of protein assemblies in crystals. Computational Life Sciences 3695 LNBI, 163–174.
Krissinel, Evgeny, Kim, Henrick, 2007. Inference of macromolecular assemblies from crystalline state. J. Mol. Biol. 372 (3), 774–797.
Kussmaul, Lothar, Hirst, Judy, 2006. The mechanism of superoxide production by NADH: ubiquinone oxidoreductase (complex I) from bovine heart mitochondria. Proc. Natl. Acad. Sci. U.S.A. 103 (20), 7607–7612.
Li, Yue, et al., 2023. Structure of human NaV1.6 channel reveals Na+ selectivity and pore blockade by 4,9-anhydro-tetrodotoxin. Nature Communications 2023 14 (1), 1–13, 1 14.
Lin, Qinghui, et al., 2017. Glutamate 52-β at Theα/β subunit interface of Escherichia coli class Ia ribonucleotide reductase is essential for conformational gating of radical transfer. J. Biol. Chem. 292 (22), 9229–9239.
Linsdell, Paul, 2017. Structural changes fundamental to gating of the cystic fibrosis transmembrane conductance regulator anion channel pore. Adv. Exp. Med. Biol. 925, 13–32.
Lofstad, Marie, et al., 2016. Activation of the class Ib ribonucleotide reductase by a flavodoxin reductase in Bacillus cereus. Biochemistry 55 (36), 4998–5001.
Mandal, Manoj, Saito, Keisuke, Ishikita, Hiroshi, 2021. Two distinct oxygen-radical conformations in the X-ray free electron laser structures of photosystem II. J. Phys. Chem. Lett. 12 (16), 4032–4037.
McCoy, Airlie J., et al., 2007. Phaser crystallographic software. J. Appl. Crystallogr. 40 (Pt 4), 658. /pmc/articles/PMC2483472/. (Accessed 30 May 2023).
McGaughey, Georgia B., Gagné, Marc, Rappé, Anthony K., 1998. π-Stacking interactions. Alive and well in proteins. J. Biol. Chem. 273 (25), 15458–15463.
Minch, Michael J., 1999. An introduction to hydrogen bonding (Jeffrey, George A.). J. Chem. Educ. 76 (6), 759.
Mowa, Mohube B., et al., 2009. Function and regulation of class I ribonucleotide reductase-encoding genes in mycobacterial. J. Bacteriol. 191 (3), 985–995.
Murshudov, Garib N., et al., 2011. REFMAC5 for the refinement of macromolecular crystal structures. Acta Crystallogr. Sect. D Biol. Crystallogr. 67 (4), 355–367.
Nilsson, Michelle, et al., 2022. An epilepsy-associated KV1.2 charge-transfer-center mutation impairs KV1.2 and KV1.4 trafficking. Proc. Natl. Acad. Sci. U.S.A. 119 (17), e2113675119.
Nordlund, Pär, Reichard, Peter, 2006. Ribonucleotide reductases. Annu. Rev. Biochem. 75, 681–706.
Nordlund, Pär, Sjöberg, Britt Marie, Eklund, Hans, 1990. Three-dimensional structure of the free radical protein of ribonucleotide reductase. Nature 345 (6276), 593–598.
Pettersen, Eric F., et al., 2004. UCSF chimera–a visualization System for exploratory research and analysis. In: Journal of Computational Chemistry, vol. 25, pp. 1605–1612, 13.
Phulera, Swastik, Mande, Shekhar C., 2013. The crystal structure of Mycobacterium tuberculosis NrdH at 0.87 Å suggests a possible mode of its activity swastik. Biochemistry 52, 5056, 4065.
Pryde, Kenneth R., Hirst, Judy, 2011. Superoxide is produced by the reduced flavin in mitochondrial complex I: a single, unified mechanism that applies during both forward and reverse electron transfer. J. Biol. Chem. 286 (20), 18056. /pmc/articles/PMC3093879/(April 4, 2024.
Roca, Ignasi, et al., 2008. NrdI essentiality for class Ib ribonucleotide reduction in Streptococcus pyogenes. J. Bacteriol. 190 (14), 4849–4858.
Romero, Elvira, et al., 2018. Same substrate, many reactions: oxygen activation in flavoenzymes. Chem. Rev. 118, 1742–1769.
Ruskoski, Terry B., Boal, Amie K., 2021. The periodic table of ribonucleotide reductases. J. Biol. Chem. 297 (4), 101137.
Sancho, J., 2006. Flavodoxins: sequence, folding, binding, function and beyond. Cell. Mol. Life Sci. 63 (7–8), 855–864.
Thomas, William C., et al., 2019. Convergent allostery in ribonucleotide reductase. Nat. Commun. 10 (1).
Torrents, Eduard, 2014. Ribonucleotide reductases: essential enzymes for bacterial life. Front. Cell. Infect. Microbiol. 4 (APR), 1–9.
Uppsten, Malin, Davis, Jamaine, Rubin, Harvey, Uhlin, Ulla, 2004. Crystal structure of the biologically active form of class Ib ribonucleotide reductase small subunit from Mycobacterium tuberculosis. FEBS (Fed. Eur. Biochem. Soc.) Lett. 569 (1–3), 117–122.
Uppsten, Malin, Färnegårdh, Mathias, Domkin, Vladimir, Uhlin, Ulla, 2006. The first holocomplex structure of ribonucleotide reductase gives new insight into its mechanism of action. J. Mol. Biol. 359 (2), 365–377.
Wang, Po Hung, Best, Robert B., Blumberger, Jochen, 2011. Multiscale simulation reveals multiple pathways for H2 and O2 transport in a [NiFe]-Hydrogenase. J. Am. Chem. Soc. 133 (10), 3548–3556.
Wörsdörfer, Bigna, Conner, Denise A., et al., 2013. Function of the diiron cluster of Escherichia coli class Ia ribonucleotide reductase in proton-coupled electron transfer. J. Am. Chem. Soc. 135 (23), 8585–8593.
Yan, Changhui, et al., 2008. Characterization of protein-protein interfaces. Protein J. 27 (1), 59–70.
Zimanyi, Christina M., et al., 2016. Molecular basis for allosteric specificity regulation in class Ia ribonucleotide reductase from Escherichia coli. Elife 5 (JANUARY2016), 1–23.